Mon. Not. R. Astron. Soc. **000**, 000–000 (2000)

Chandra measurements of the distribution of mass in the luminous lensing cluster Abell 2390

S.W. Allen, S. Ettori and A.C. Fabian
Institute of Astronomy, Madingley Road, Cambridge CB3 OHA

September 2, 2000

ABSTRACT

We present spatially-resolved X-ray spectroscopy of the luminous lensing cluster Abell 2390, using observations made with the Chandra observatory. The temperature of the X-ray gas is shown to rise with increasing radius within the central ~ 200 kpc of the cluster, and then remains approximately isothermal, with $kT = 11.5^{+1.5}_{-1.6}$ keV, out to the limits of the observations at $r \sim 1.0$ Mpc. The total mass profile determined from the Chandra data has a form in good agreement with the predictions from numerical simulations. Using the parameterization of Navarro, Frenk & White (1997), we measure a scale radius $r_{\rm s} \sim 0.7$ Mpc and a concentration parameter $c \sim 5$. The best-fit X-ray mass model is in excellent agreement with independent measurements from strong and weak lensing studies and optical measurements of the galaxy velocity dispersion in the cluster. The X-ray gas-to-total-mass ratio rises with increasing radius within the central ~ 0.7 Mpc with $f_{\rm gas} \propto r^{0.3}$. At $r = 0.9$ Mpc, we measure $f_{\rm gas} = 15.7^{+5.6}_{-4.1}$ per cent (90 per cent confidence limits). The azimuthally-averaged $0.3 - 7.0$ keV surface brightness profile exhibits a small core radius and a clear 'break' at $r \sim 500$ kpc, where the slope changes from $S_{\rm X} \propto r^{-1.4}$ to $S_{\rm X} \propto r^{-3.7}$. The data for the central ~ 70 kpc radius indicate the presence of a strong cooling flow with a mass deposition rate of $200 - 250$ $\rm M_{\odot}\,yr^{-1}$ and an age of ~ 3 Gyr.

Key words: galaxies: clusters: individual: Abell 2390 – cooling flows – intergalactic medium – gravitational lensing – X-rays: galaxies

1 INTRODUCTION

Accurate measurements of the masses of clusters of galaxies are of profound importance to cosmological studies. Originally, most measurements of cluster masses were based on optical studies of their galaxy dynamics, wherein the motions of individual galaxies were used to trace the cluster potentials. Although such studies were shown to be sensitive to systematic uncertainties due to velocity anisotropies, substructure and projection effects (*e.g.* Lucey 1983; Frenk *et al.* 1990; van Haarlem, Frenk & White 1997), more recent work based on large galaxy samples and employing careful selection techniques, has lead to significant progress (*e.g.* Carlberg *et al.* 1996; den Hartog & Katgert 1996; Fadda *et al.* 1996; Mazure *et al.* 1996; Borgani *et al.* 1999; Geller, Diaferio & Kurtz 1999; Koranyi & Geller 2000).

Recent years have also seen the development of two further techniques for measuring the masses of clusters, based on X-ray observations and studies of gravitational lensing by clusters, respectively. X-ray mass measurements use the assumption that the X-ray emitting gas which pervades clusters is in hydrostatic equilibrium; the total mass distribution is determined once the radial distributions of the X-ray gas density and temperature are known (see *e.g.* Sarazin 1988). Since the X-ray emissivity is proportional to the square of the gas density, and the relaxation timescale for the X-ray gas is relatively short (of the order of a few sound crossing times), the X-ray method is relatively free from the projection and substructure effects which hamper the aforementioned optical studies.

In contrast to the X-ray and optical dynamical techniques, gravitational lensing offers a method for measuring the projected masses through clusters that is essentially free from assumptions about the dynamical state of the gravitating matter (see *e.g.* Fort & Mellier 1994; Bartelmann & Schneider 1999; Mellier 1999 for reviews). The primary observational challenges of requiring deep exposures, excellent seeing conditions, wide field imaging and accurate point spread function models have now been largely overcome with improved instrumentation (*e.g.* Bacon *et al.* 2000 and references therein), although the recovery of the three-dimensional mass distributions in clusters can be complicated by projection effects and uncertainties in the redshift distributions of the lensed sources.

Clearly, the best approach when attempting to reliably measure the masses of clusters is to combine these three methods. The first combined X-ray and lensing studies of

galaxy clusters (Miralda-Escudé & Babul 1995) suggested that strong lensing masses, measured within $r \lesssim 200$ kpc of the cluster centre, might typically overestimate X-ray-determined masses by a factor of $\sim 2-3$. This sparked debate into the possible effects of oblate/prolate cluster geometries, projection effects, complex temperature structures and pressure support from bulk and/or turbulent motions and magnetic fields in the X-ray gas (*e.g.* Miralda-Escudé & Babul 1995; Loeb & Mao 1994; Waxman & Miralda-Escudé 1995; Kneib *et al.* 1995; Bartelmann & Steinmetz 1996). Later work (Allen, Fabian & Kneib 1996; Allen 1998; Böhringer *et al.* 1998; Wu 2000) highlighted a clear difference between the results obtained for cooling-flow (hereafter CF) and non-cooling flow (NCF) clusters. For CF clusters, the X-ray and strong lensing mass measurements generally show good agreement, once the effects of the cooling flows are accounted for in the X-ray analysis. For NCF systems, however, the masses inferred from the strong lensing data invariably exceed the X-ray values, determined under the hydrostatic assumption, by a factor of $2-4$.

The origin of the different results obtained for CF and NCF clusters is thought to lie in the different dynamical states of these systems: whereas X-ray and optical imaging and detailed lensing analyses of CF clusters show them to be regular and dynamically-relaxed systems, NCF clusters generally appear to be undergoing major subcluster merger events (*e.g.* Edge, Stewart & Fabian 1992; Buote & Tsai 1996; Kneib *et al.* 1995; Smail *et al.* 1995, 1997; Squires *et al.* 1997). Significant offsets between the X-ray and lensing centroids are observed in NCF clusters, demonstrating a loss of hydrostatic equilibrium in their central regions. The X-ray core radii for NCF systems also appear to have been inflated by the dynamical activity, in agreement with the predictions from numerical simulations (*e.g.* Roetigger *et al.* 1996); this inflation of the X-ray core radii can account for the X-ray/strong lensing mass discrepancy in most NCF systems (Allen 1998). On larger spatial scales ($r \gtrsim 0.5$ Mpc), comparisons between weak lensing, X-ray and optical dynamical mass measurements generally provide a consistent picture, with excellent agreement between the results obtained for both CF and NCF clusters (*e.g.* Squires *et al.* 1996; Smail *et al.* 1997; Wu & Fang 1997; Allen 1998; Lewis *et al.* 1999). This suggests that the loss of hydrostatic equilibrium in NCF clusters is primarily restricted to their inner regions.

The most significant uncertainty associated with the X-ray mass measurements in previous joint X-ray/lensing studies has been the absence of any direct measurements of the X-ray temperature profiles in the clusters, which impacts directly on the mass measurements through the hydrostatic equation. Although limited spatially-resolved spectroscopy for bright, nearby clusters was possible using ASCA and Beppo-SAX observations (*e.g.* Markevitch *et al.* 1998; Kikuchi *et al.* 1999; de Grandi & Molendi 1999; White 2000; Irwin & Bregman 2000), for the more distant lensing clusters, typically observed at redshifts $z \gtrsim 0.2$, only a single, integrated cluster spectrum was normally available. In most cases, only a mean emission-weighted X-ray temperature was therefore determined, although more sophisticated studies also accounted for the effects of cooling flows on the X-ray data (*e.g.* Allen 1998; Böhringer *et al.* 1998). For the mass analyses, it was then necessarily assumed that the mass-weighted temperature profile followed some particular form, and usually that it remained approximately isothermal with radius. However, the validity of this assumption remains uncertain, especially within the strong lensing regime.

The launch of the Chandra Observatory (Weisskopf *et al.* 2000) in 1999 July provides the first opportunity for detailed, spatially-resolved X-ray spectroscopy of clusters of galaxies at moderate redshifts. The Advanced CCD Imaging Spectrometer (ACIS) on Chandra permits the first direct, simultaneous measurements of the X-ray temperature and density profiles and, via the hydrostatic assumption, the mass distribution in luminous lensing clusters, spanning both the weak and strong lensing regimes. In this paper we present the first results from Chandra observations of the massive CF lensing cluster Abell 2390, which has been the subject of several previous combined X-ray/optical/lensing studies (*e.g.* Piere *et al.* 1996, Squires *et al.* 1996, Allen 1998, Böhringer *et al.* 1998, Lewis *et al.* 1999). We present detailed results on the mass distribution in the cluster determined from the Chandra data and compare our results with those from detailed strong and weak lensing analyses and optical dynamical studies. We also re-examine the properties of the cooling flow in the cluster and discuss their relation to the dynamical history of the system.

The cosmological parameters H_0=50 $\mathrm{km\,s^{-1}\ Mpc^{-1}}$, $\Omega = 1$ and $\Lambda = 0$ are assumed throughout. At the redshift of Abell 2390 ($z = 0.2301$), an angular scale of 1 arcsec corresponds to a physical length of 4.652 kpc.

2 OBSERVATIONS

The Chandra observations of Abell 2390 were carried out using the ACIS on 1999 November 7. The target was observed in the back-illuminated CCD detectors, close to the nominal aim point for the ACIS S3 detector. (The source was positioned near the centre of node-1 on the chip). The focal plane temperature at the time of the observations was -110C.

We have used the CIAO software (version 1.3) and the level-2 events file provided by the standard Chandra pipeline processing for our analysis. The light curve for the observation was of high quality with no strong background flaring. Only those X-ray events with grade classifications of 0,2,3,4 and 6 were included in our final cleaned data set, for which the net exposure time was 9.13ks.

3 X-RAY IMAGING ANALYSIS

3.1 X-ray morphology

The raw $0.3-7.0$ keV image of the central 6×6 arcmin^2 (1.8×1.8 Mpc^2) region of Abell 2390 is shown in Fig. 1(a). The pixel size is 1.97×1.97 arcsec^2, corresponding to 4×4 raw detector pixels. Fig. 1(b) shows an adaptively smoothed version of the same image, using the smoothing algorithm of Ebeling, White & Rangarajan (2000). The position of the peak of the X-ray emission from the cluster, 21h53m36.77 +17d41m42.8s (J2000.), is in excellent agreement with the optical centroid for the dominant cluster galaxy of 21h53m36.76 +17d41m42.9s (J2000.; Pierre *et al.* 1996). The X-ray image is elongated along an approximately

northwest-southeast direction, in a similar manner to the optical isophotes of the dominant galaxy (Pierre *et al.* 1996).

Some substructure is apparent in the Chandra image. In the central region, a relatively bright ridge of enhanced emission extends $\sim 3-4$ arcsec to the northwest of the X-ray peak (Fig. 2). Enhanced emission in the same direction is also observed in the optical blue continuum and optical/UV line emission from the dominant cluster galaxy (Lémonon *et al.* 1998; Edge *et al.* 1999; Hutchings & Balogh 2000). A correspondence between the brightest X-ray emission with excess blue continuum and optical/UV line emission (probably associated with the formation of young, massive stars) is also observed in the nearby CF clusters Hydra-A (McNamara *et al.* 2000) and Abell 1795 (Fabian *et al.* 2000b). A second, fainter region of enhanced X-ray emission extends ~ 6 arcsec to the south-southeast.

On medium ($\sim$ 1 arcmin) scales, the X-ray emission is extended to the west-northwest, in a similar manner to the lensing mass model of Piere *et al.* (1996; these authors also note the presence of an X-ray extension in the same direction using ROSAT High Resolution Imager data). On large scales ($\gtrsim$ 2 arcmin) the X-ray emission is extended towards the east. The presence of such substructure in the Chandra image suggests that the cluster has not fully relaxed following it's most recent merger activity. However, the agreement between the X-ray, optical and gravitational lensing mass measurements discussed in Section 5.2 argues strongly that the assumption of hydrostatic equilibrium in the cluster is a reasonable one.

Three point sources are detected to the west of the X-ray peak, in the central regions of the cluster, at positions 21h53m33.19 +17d42m08.4s, 21h53m33.74 +17d41m13.3s, and 21h53m34.02 +17d42m39.9s. The X-ray and sub-mm properties of these sources are discussed by Fabian *et al.* (2000a). Four more point sources are also visible at larger radii in Fig. 1(b).

3.2 The surface brightness profile

The azimuthally-averaged, $0.3-7.0$ keV X-ray surface brightness profile for Abell 2390 is shown in Fig. 3. The profile has been flat-fielded and background subtracted using a rectangular background region of size 400×50 arcsec^2, located ~ 5 arcmin from the cluster centre. All obvious point sources were excluded from the analysis.

The X-ray emission from the cluster extends beyond the 5 arcmin ($\sim$ 1.4 Mpc) radius associated with our on-chip background region (see also Pierre *et al.* 1996; Böhringer *et al.* 1998). However, beyond this radius background counts dominate the flux in the ACIS-S3 detector. Fig. 3 shows the data for the central 900 kpc (193 arcsec), for which systematic errors associated with the background subtraction and flat fielding are negligible. The bin-size in Fig. 3(a) is 2 detector pixels (0.984 arcsec). Fig. 3(b) shows the data for the outer regions of the cluster with a larger binsize of 8 detector pixels (3.94 arcsec).

Within a radius of 500 kpc (107 arcsec), the X-ray surface brightness profile can be parameterized ($\chi^2 = 127$ for 106 degrees of freedom) by a standard β-model (*e.g.* Jones & Forman 1984) of the form $S(r) = S(0)\left[(1+r/r_{\rm c})^2\right]^{1/2-3\beta}$, with a core radius $r_{\rm c} = 30.1\pm1.5$ kpc and a slope parameter $\beta = 0.408\pm0.003$ (1σ errors; $\Delta\chi^2 = 1.0$). On larger scales, however, the β-model does not provide an acceptable fit: examining the data for the central 900 kpc radius, we obtain $\chi^2 = 920$ for 194 degrees of freedom, with best-fit parameter values of $r_{\rm c} = 62$ kpc and $\beta = 0.48$). Ignoring the central $\sim$ 80 kpc (18 arcsec) region occupied by the cooling flow (Section 6.2), the fit is improved ($\chi^2 = 473$ for 177 degrees of freedom, with best-fit parameter values $r_{\rm c} = 172$kpc and $\beta = 0.59$) although is still formally unacceptable.

The main reason for the poor fit obtained with the β-model at larger radii is the presence of a 'break' in the surface brightness profile at $r \sim 500$ kpc (Fig. 3b). This break is not obviously due to substructure in any particular direction in the cluster: Fig. 4 shows the surface brightness profile measured in the four quadrants covering position angles $45-135$, $135-225$, $225-315$ and $315-45$ degrees. We see that profile appears remarkably similar in three of the four directions, although the emission is slightly more extended towards the east (as is also evident in the images presented in Fig. 1).

A good fit to the surface brightness profile beyond the central cooling region can be obtained using a simple broken power-law model. Fitting the data from $80-900$ kpc, we obtain $\chi^2 = 169$ for 176 degrees of freedom, with a break at a radius of 496^{+8}_{-14} kpc, and slopes in the regions internal and external to the break radius of -1.44 ± 0.02 and -3.71 ± 0.16, respectively. Interestingly, these slopes are similar to the values expected at small and large radii for the dark matter in a Navarro, Frenk & White (1997; hereafter NFW) potential in which $\rho \propto 1/((r/r_{\rm s})(1+r/r_{\rm s})^2)$. However, isothermal gas in an NFW-like potential should not exhibit a sharp break at the scale radius $r_{\rm s}$, but rather a slow rollover (although individual clusters in the simulations presented by Thomas *et al.* 2000 do exhibit sharp breaks in their dark matter distributions). Fitting the surface brightness profile external to the cooling flow ($80-900$ kpc) with the prescription for isothermal gas in an NFW potential described by Ettori & Fabian (1999), we measure $r_{\rm s} = 660^{+60}_{-50}$ kpc (1σ errors), with $\chi^2 = 403$ for 177 degrees of freedom. Thus, the fit with the NFW mass model assuming strict isothermality in the X-ray gas is formally unacceptable, although provides a better description of the data in the $80-900$ kpc region than the β-model. As discussed in Section 4, the Chandra data show that the X-ray gas in Abell 2390 is not isothermal and that the temperature rises with increasing radius within the central ~ 200 kpc. In Section 5 we show that an NFW mass model can provide a reasonable description of the Chandra data, once the assumption of isothermality is relaxed.

4 SPATIALLY-RESOLVED SPECTROSCOPY

4.1 Method of analysis

For our spectral analysis, we divided the cluster into annular regions, as detailed in Table 1. A spectrum was extracted from each region in 1024 Pulse Height Analyser (PHA) channels. The spectra were re-grouped to contain a minimum of 20 counts per PHA channel, thereby allowing χ^2 statistics to be used. (For the two outer annuli, a larger grouping of 40 counts per PHA channel was used, due to the increased background contribution). Background spectra, appropriate

for the regions studied, were extracted from the ACIS-S3 blank-field data sets available from the Chandra X-ray Center. All obvious point sources were masked out and excluded from the analysis. Separate photon-weighted response matrices and effective area files were constructed for each region using the calibration and response files appropriate for the focal plane temperature, available from the Chandra X-ray Centre.

Two separate energy ranges were examined. Firstly, a conservative $0.5-7.0$ keV band was used over which the calibration of the back-illuminated CCD detectors is currently best understood. Secondly, for the central 100 kpc region where a strong cooling flow is thought to exist (Section 6), we have also examined a more extended $0.3-7.0$ keV energy range, which provides extra constraints on the presence of cool emission components and/or intrinsic absorption in the cluster.

4.2 The spectral models

The analysis of the spectral data has been carried out using the XSPEC software package (version 11.01; Arnaud 1996). The spectra were modeled using the plasma emission code of Kaastra & Mewe (1993; incorporating the Fe L calculations of Liedhal, Osterheld & Goldstein 1995) and the photoelectric absorption models of Balucinska-Church & McCammon (1992). We first examined each annular spectrum using a simple, single-temperature model with the absorbing column density fixed at the nominal Galactic value ($N_{\rm H} = 6.8\times10^{20}$atom cm^{-2}; Dickey & Lockman 1990). This model is hereafter referred to as model A. The free parameters in model A were the temperature (kT) and metallicity (Z) of the plasma (measured relative to the solar photospheric values of Anders & Grevesse 1989, with the various elements assumed to be present in their solar ratios) and the emission measure (K). We also examined a second single-temperature model (model B) which was identical to model A but with the absorbing column density ($N_{\rm H}$) also included as a free parameter in the fits.

The image deprojection and X-ray colour profile analyses discussed in Sections 5 and 6 indicate the presence of a strong cooling flow in the central $r \lesssim 100$ kpc region of the cluster. We have therefore also examined the spectral data for this region using a series of more sophisticated, multiphase models in which the emission properties of the cooling flow were explicitly accounted for. The first such model (model C1) introduced an extra emission component into model A, with a spectrum appropriate for gas cooling at constant pressure from the ambient cluster temperature (following the prescription of Johnstone *et al.* 1992). The normalization of this component was parameterized in terms of a mass deposition rate, $\dot{M}$, which was a free parameter in the fits. In the second case, model C2, the cooling gas was modelled as an isothermal cooling flow, following Nulsen (1998; we assume a value for $\eta = 1$, where the integrated mass deposition rate within radius r, $\dot{M} \propto r^{\eta}$). The mean gas temperature and metallicity in both the cooling flow and isothermal emission component (which accounts for the emission from gas at larger radii viewed in projection) were assumed to be equal. Finally, we also examined a more general emission model, model D, in which the cooling gas was modelled by a second, cooler isothermal emission component, with the temperature and normalization of this component included as free fit parameters. Model D provides a more flexible parameterization, with an additional degree of freedom over models C1 and C2, and invariably provides a good match to the more specific cooling-flow models at the spectral resolution and signal-to-noise ratios typical of ACIS cluster observations. However, the parameter values determined with model D were not well constrained for Abell 2390, and thus we do not quote explicit results for this model here.

With each of the cooling-flow emission models, we have also examined the effects of including extra absorption, using a variety of different absorption models. In the first case (absorption model i), the only absorption included was that due to cold gas in our Galaxy, with the equivalent column density fixed to the nominal Galactic value (Dickey & Lockman 1990; For a single temperature emission model, this is identical to spectral model A). In the second model (model ii), the absorption was again assumed to be due to Galactic (zero redshift) cold gas, but with the column density, $N_{\rm H}$, included as a free parameter in the fits. (For a single temperature emission model, this would be equivalent to spectral model B.) In the third case (absorption model iii), an intrinsic absorption component with column density, $\Delta N_{\rm H}$, due to cold gas at the redshift of the cluster was introduced. The absorber was assumed to lie in a uniform screen in front of the cooling flow, with the column density included a free fit parameter. In the fourth case (model iv), the intrinsic absorption was assumed to cover only a fraction, f, of the emission from the cooling flow. The fifth and final absorption model (model v) was similar to model (iii) but with the gaseous absorber replaced by an intrinsic absorption edge, with the edge depth, τ, and energy, $E_{\rm edge}$, free parameters in the fits. This more general absorption model may be used to approximate the effects of a dusty and/or ionized absorber.

In those cases where the absorption has been quantified in terms of an equivalent hydrogen column density, solar metallicity in the absorbing gas is assumed. We note that in absorption models (iii–v), the absorption acting on the ambient cluster emission was fixed at the nominal Galactic value. However, allowing the Galactic absorption to vary from this value did not significantly improve the fits.

4.3 Results from the single-phase analysis

The best-fit parameter values and 1σ ($\Delta\chi^2 = 1.0$) and 90 per cent ($\Delta\chi^2 = 2.71$) confidence limits determined from the fits in the $0.5-7.0$ keV band with the single temperature models are summarized in Tables 1 and 2. The temperature profile determined with spectral model A is shown in Fig. 5(a). The measured temperature is approximately isothermal beyond a radius of 200 kpc, out to the limits of the data at $r \sim 1$ Mpc. A combined fit to the data in the $0.2-1.0$ Mpc range with model A gives a mean temperature of $11.5^{+1.6}_{-1.3}$ keV. Fitting the $0.2-1.0$ Mpc results with a simple power-law model of the form $kT \propto r^{\alpha}$ we measure $\alpha = 0.0 \pm 0.2$ (1σ bootstrap errors obtained using the Akritas & Bershady 1996 modification of the ordinary least squares statistic.) We observe a clear drop in the emission weighted temperature within the central 100 kpc, which is

in part due to the presence of the cooling flow (see Section 4.4, below).

We detect marginal evidence for a metallicity gradient in the cluster, with a mean, best-fit value for the central 100 kpc of $Z = 0.48^{+0.11}_{-0.10} Z$, which compares to a mean value of $0.23^{+0.12}_{-0.13} Z$ for the outer $0.2 - 1.0$ Mpc region (Fig. 6a; 1σ errors). The results determined with spectral model B in the $0.5 - 7.0$ keV band also provide marginal evidence for increased absorption towards the cluster core (Fig. 6b).

In all cases, the χ^2 values obtained from the fits to the $0.5 - 7.0$ keV data with the single-temperature models are acceptable, the only marginal case being the data for the central 50 kpc region, where the spectrum is complicated by the effects of the cooling flow.

4.4 Multiphase analysis of the cooling core

The results determined from the more detailed, multiphase analysis of the central 100 kpc radius in the extended $0.3-7.0$ keV energy band are summarized in Table 3. The results demonstrate a clear requirement for excess absorption in this central region, over and above the nominal Galactic value (Dickey & Lockman 1990), using each of the different emission models. The systematic variations between the column density measurements obtained with the different emission and absorption models are similar to those determined from previous ASCA studies (*e.g.* Allen 2000). Unfortunately, the present Chandra data for Abell 2390 cannot statistically discriminate between the single-phase and multiphase emission models for the central 100 kpc region, which provide comparable χ^2 values with each absorption model. (We note, however, that at some level the projected spectrum for the central 100 kpc must be multiphase, simply given the results on the temperature profile in Fig. 5(a).)

For our preferred cooling-flow emission models including intrinsic absorption, which provide the most consistent physical description of the spectral and imaging data (Section 6), we measure an integrated mass deposition rate in the central 100 kpc region, $\dot{M} = 200 - 300$ $\mathrm{M_\odot\ yr^{-1}}$.

Fig. 5(b) shows the projected temperature profile for Abell 2390, corrected for the effects of the cooling flow in the central region using spectral model C2(iii; at larger radii the results determined with spectral model A in the $0.5-7.0$ keV band have been used). We see that once the effects of the cooling flow have been accounted for, the temperature drop in the central regions is reduced with respect Fig. 5(a), but not entirely eliminated. Assuming that the isothermal cooling flow model provides a reasonable description of the data, the residual drop in the ambient (mass-weighted) temperature profile in the central 100 kpc shown in Fig. 5(b) should directly reflect the mass distribution in the cluster core.

The data for Abell 2390 do not provide firm constraints on the nature of the intrinsic absorption in the cluster. Using the partial-covering absorption model (iv), we find that high covering fractions are preferred. For the edge-like absorption model (v), the lower limit on the edge energy is essentially unconstrained: for emission models C1(v) and C2(v), however, the upper limit on the edge energy is inconsistent with the OI K edge of oxygen ($E_{\rm edge} \sim 0.54$ keV), suggesting that the absorption is unlikely to be due to oxygen rich dust grains (*e.g.* Arnaud & Mushotzky 1998; Allen *et al.* 2000b) or a warm, ionized absorber (Buote 2000).

Assuming that the intrinsic absorption is due to cold gas lying in a uniform screen in front of the cooling flow, using spectral model C2(iii), we measure $\Delta N_{\rm H} = 2.2^{+1.1}_{-0.8} \times 10^{21}$ atom cm^{-2}. The mass of absorbing gas implied this model is then $M_{\rm abs} \sim 3 \times 10^7 r^2_{\rm abs} \Delta N_{\rm H}\, \mathrm{M_\odot}$, where $r_{\rm abs}$ is the radial extent of the absorber in kpc and $\Delta N_{\rm H}$ is the equivalent hydrogen column density in units of 10^{21} atom cm^{-2}. For $r_{\rm abs} \sim 70$ kpc (Section 6.2) we obtain $M_{\rm abs} \sim 3.2^{+1.6}_{-1.2} \times 10^{11}$ $\mathrm{M_\odot}$ (although Allen & Fabian 1997 and Wise & Sarazin 2000 argue that for a more reasonable geometry, in which the absorbing material is distributed throughout the X-ray emitting region, the true mass is likely to be a few times higher). This mass is in reasonable agreement with the mass expected to have been accumulated by the cooling flow within the same radius over its lifetime; $\sim \dot{M}t/2 \sim 3.5 \times 10^{11}$ $\mathrm{M_\odot}$ (the factor two in the denominator arises from the assumption that the integrated mass deposition rate, $\dot{M}$, grows approximately linearly with time).

4.5 Spectral deprojection analysis.

In order to determine the three-dimensional temperature profile in the cluster, we have carried out a simple deprojection analysis of the spectral results on the projected temperature and emission measure profiles determined above. (For the outer regions of the cluster, the results determined with spectral model A were used. For the central 100 kpc, the results determined with spectral model C2(iii) were preferred.) For this analysis, we divided the cluster into concentric spherical shells, defined by the annular regions listed in Table 1. For the outermost shell, the temperature and density can be determined directly from the temperature and emission measure in the projected annular spectrum. (We ignore corrections for the emission from larger radii, which are negligible for all but the outermost shell.) Under the assumption of spherical symmetry, the contribution from the outermost shell to the projected emission in each inner annulus is then determined by purely geometric factors. Accounting for this contribution to the second annulus inward, we can determine the mean gas temperature and density in the second spherical shell and so forth, working inward.

The deprojected temperature profile determined by this method is shown in Fig. 7. The results for the outer regions of the cluster have been lightly smoothed in order to reduce the appearance of noise. The (1σ) errors bars have been estimated using a Monte Carlo technique.

4.6 Comparison with previous work

The mean ambient temperature for Abell 2390 of $kT = 11.5^{+1.6}_{-1.3}$ keV, determined from the combined analysis of the data in the $0.2 - 1$ Mpc range, is in good agreement with the previous results of $kT = 14.5^{+15.5}_{-5.2}$keV from Allen (1998) based on ASCA observations, and $kT = 11.1^{+1.5}_{-1.6}$ keV from Böhringer *et al.* (1998), based on a joint analysis of ASCA and ROSAT Position Sensitive Proportional Counter (PSPC) data. (Both Allen 1998 and Böhringer *et al.* 1998 accounted for the effects of the central cooling flow in their modelling of the integrated cluster spectra. Using a simpler,

single-temperature emission model, Böhringer *et al.* (1998) measured a lower mean emission-weighted temperature of $kT \sim 9$ keV.) The ambient temperature for Abell 2390 measured with Chandra is also in good agreement with the predicted value of ~ 12.0 keV using the cooling-flow corrected $kT_{\rm X}/L_{\rm Bol}$ relation of Allen & Fabian (1998; we assume a bolometric luminosity of $\sim 1.0 \times 10^{46}$ erg s^{-1} as measured by ASCA since the Chandra observations do not cover the whole of the cluster).

The best-fit mass deposition rate from the cooling flow of $\dot{M} \sim 200 - 300$ M$_\odot$ yr^{-1}, determined from the Chandra spectrum for the central 100 kpc region, is lower than previous measurements based on the analysis of integrated spectra for the whole cluster from ASCA ($\dot{M} = 1500^{+600}_{-1100}$ M$_\odot$ yr^{-1}; Allen 2000), joint ASCA/ROSAT ($\dot{M} = 700^{+150}_{-300}$ M$_\odot$ yr^{-1}; Böhringer *et al.* 1998) and Beppo-SAX ($\dot{M} = 700^{+400}_{-300}$ M$_\odot$ yr^{-1}; Ettori, Allen & Fabian 2000), observations (although the results are marginally consistent at the ~ 95 per cent confidence level). In part, this difference is likely to be due to the fact that the ambient gas temperature in the centre of the cluster, corrected for the effects of the cooling flow, is lower than the mean value measured at larger radii (Fig. 5b). If this drop in the central ambient temperature is not accounted for (as was the case in the previous ASCA and BeppoSAX studies, which could not spatially resolve the cooling flow from the hotter, outer cluster gas) then the cooler, ambient gas in the cluster core will also tend to be modelled as part of the cooling flow, and the total mass deposition rate will be overestimated. This effect is illustrated by the fact that a fit with spectral model C2(iii) to a single Chandra spectrum covering the entire central 500 kpc (radius) of the cluster, gives $\dot{M} = 621^{+121}_{-113}$ M$_\odot$ yr^{-1}, $\Delta N_{\rm H} = 1.6^{+0.8}_{-0.6} \times 10^{21}$atom cm^{-2} and $kT = 11.9^{+4.2}_{-1.9}$ keV, in good agreement with the previous ASCA, ROSAT and BeppoSAX results. * However, a fit to the central 200 kpc radius region (the maximum possible size of any cooling flow; Section 6) gives $\dot{M} = 280 \pm 110$ M$_\odot$ yr^{-1} ($kT = 8.6^{+1.3}_{-0.9}$ keV), in good agreement with the value listed in Table 3. These results, and the consistent findings from the spectral, image deprojection and X-ray colour profile analyses of the innermost 100kpc presented in Section 6, highlight the need for detailed spatially-resolved spectroscopy when attempting to study the properties of cooling flows in distant clusters.

Finally, we note that the excess column density acting on the cooling flow component measured with spectral model C1(iii) of $\Delta N_{\rm H} = 2.4^{+1.2}_{-0.9} \times 10^{21}$atom cm^{-2} is consistent with the previous measurement of $2.9^{+7.6}_{-1.5} \times 10^{21}$atom cm^{-2} from ASCA, using the same model (Allen 2000).

* Although the fit with spectral model C2(iii) to the Chandra spectrum for the central 500 kpc (radius) region overestimates the mass deposition rate from the cooling flow, the measured temperature is in good agreement with the true value at large radii in the cluster (Fig. 5b). Thus, previous ASCA and Beppo-SAX studies which attempted to account for the effects of cooling flows on integrated cluster spectra (*e.g.* Allen 1998; Böhringer *et al.* 1998) may have overestimated the mass deposition rates from the cooling flows but are likely to have provided reasonable estimates for the mean cluster temperatures.

5 MEASUREMENT OF THE CLUSTER MASS PROFILE

5.1 The mass model

The observed X-ray surface brightness profile (Fig. 3a) and ambient gas temperature profile (Figs. 5b, 7) may together be used to determine the X-ray gas mass and total mass profiles in the cluster. For this analysis, we have used an updated version of the deprojection code of Fabian *et al.* (1981; see also White, Jones & Forman 1997 for details). A variety of simple parameterizations for the cluster mass distribution were examined, to establish which could provide an adequate description of the Chandra data. For those mass models providing reasonable fits, the best-fit parameter values were determined using a simple iterative technique.† Spherical symmetry and hydrostatic equilibrium are assumed throughout.

We find than an excellent fit to the Chandra data can be obtained using an NFW mass model

$$\rho(r) = \frac{\rho_{\rm crit}\delta_{\rm c}}{(r/r_{\rm s})\,(1+r/r_{\rm s})^2}, \qquad (1)$$

where $\rho(r)$ is the mass density, $\rho_{\rm crit} = 3H^2/8\pi G$ is the critical density for closure and

$$\delta_{\rm c} = \frac{200}{3}\frac{c^3}{[\ln(1+c) - c/(1+c)]}, \qquad (2)$$

with a scale radius, $r_{\rm s} \sim 0.7$ Mpc (in agreement with the value determined from the fit to the surface brightness profile under the isothermal gas assumption in Section 3.2) and a concentration parameter, $c = 5.1 \pm 0.5$ (90 per cent confidence limits). The normalization of the mass profile may also be expressed in terms of an equivalent velocity dispersion, $\sigma = \sqrt{50} H_0 r_{\rm s} c$ (with $r_{\rm s}$ in units of Mpc). The equivalent velocity dispersion associated with the best-fit X-ray mass model of $\sigma = 1260^{+130}_{-110}$ km s^{-1}, is in excellent agreement with the robust, optically-determined value of 1262^{+89}_{-68} km s^{-1} from Borgani *et al.* (1999; from a re-analysis of the data of Carlberg *et al.* 1996 and references therein). Note that the errors on the concentration parameter and equivalent velocity dispersion quoted above are the maximum and minimum values which give rise to luminosity-weighted temperatures in the $0.2 - 1.0$ Mpc range that are consistent with the observed 90 per cent confidence limits from the Chandra data ($kT = 11.5^{+1.6}_{-1.3}$ keV), assuming a fixed value for the scale radius, $r_{\rm s} = 0.7$ Mpc. However, the best-fit values of c and $r_{\rm s}$ are correlated and acceptable fits to the Chandra data can be obtained for any $r_{\rm s}$ value $\gtrsim 0.4$Mpc, although the best-fit mass distributions within the central 1Mpc are similar in all cases. (Fixing $r_{\rm s} = 0.4$ Mpc in the NFW mass model, we obtain a best-fit concentration parameter $c = 7.7 \pm 0.7$ and an equivalent velocity

† Given the observed surface brightness profile and a particular parameterized mass model, the deprojection code is used to predict the temperature profile of the X-ray gas, which is then compared with the observations. The parameters for the mass model are stepped through a regular grid of values to determine which provide the best fit to the observed temperature profile (Fig. 7). Uncertainties on the predicted temperature profiles are determined using a Monte-Carlo technique.

dispersion $\sigma = 1090^{+100}_{-90}$ km s^{-1} . For $r_s = 1.0$ Mpc, we obtain $c = 4.0 \pm 0.4$ and $\sigma = 1410^{+150}_{-130}$ km s^{-1} .)

The best-fit NFW mass model, with $r_s = 0.7$ Mpc and $c = 5.1 \pm 0.5$ has a virial radius $r_{200} = cr_s = 3.57 \pm 0.35$ Mpc and an integrated mass within this radius, $M_{200} = 2.63^{+0.89}_{-0.64} \times 10^{15}$ M$_\odot$. (For $r_s = 0.4$ Mpc and $c = 7.7 \pm 0.7$ we obtain $r_{200} = 3.08 \pm 0.28$ Mpc and $M_{200} = 1.70^{+0.51}_{-0.39} \times 10^{15}$ M$_\odot$. For $r_s = 1.0$ Mpc and $c = 7.7 \pm 0.7$ we obtain $r_{200} = 4.0 \pm 0.4$ Mpc and $M_{200} = 3.70^{+1.28}_{-0.95} \times 10^{15}$ M$_\odot$.)

The X-ray gas temperature profile implied by the best-fitting mass model (given the observed surface brightness profile) is shown overlaid on the deprojected spectral results in Fig. 7. The agreement between observed and predicted values is good, indicating that the NFW mass model provides a reasonable description of the Chandra data.

5.2 Comparison of X-ray and lensing mass measurements

Abell 2390 is one of the best studied lensing clusters (*e.g.* Pelló *et al.* 1991; Kassiola, Kovner & Blandford 1992; Narasimha & Chitre 1993; Pierre *et al.* 1996; Squires *et al.* 1996; Bezecourt & Soucail 1997; Frye & Broadhurst 1998; Pello *et al.* 1999). The cluster exhibits an unusual, strongly lensed 'straight arc' approximately 38 arcsec (174 kpc) away from the nucleus of the central galaxy (Pelló *et al.* 1991) in addition to many other arcs and arclets (*e.g.* Bezecourt & Soucail 1997; Pelló *et al.* 1999). Pierre *et al.* (1996) present a two-component mass model for the central regions of the cluster and measure a projected mass within the radius defined by the brightest arc of $1.6 \pm 0.2 \times 10^{14}$ M$_\odot$. Squires *et al.* (1996) present a weak lensing analysis of the cluster and determine an azimuthally averaged mass profile covering the central ~ 4.3 arcmin (1.2 Mpc).

Fig. 8 shows the projected mass profile determined from the Chandra X-ray data, with the Squires *et al.* (1996) weak lensing results and Piere *et al.* (1996) strong lensing results overlaid. For the X-ray analysis, we assume that the best-fit NFW mass model extends to an outer radius of 3.5 Mpc, approximately equal to the virial radius for the cluster. The agreement between the X-ray and lensing mass results in Fig. 8 is good at all radii studied. The mean scatter of the lensing results about the best-fit X-ray mass profile in the central 1 Mpc region is 17 per cent. The agreement of the independent lensing and X-ray mass measurements, together with the excellent agreement between the equivalent X-ray and observed optical galaxy velocity dispersions, strongly suggests that the mass profile in Abell 2390 has been robustly determined. Our results confirm the validity of the hydrostatic assumption used in the X-ray analysis and indicate that any non-thermal pressure support of the X-ray gas on these scales must be small.

5.3 The X-ray gas mass fraction

The X-ray gas mass to total mass ratio as a function of radius, $f_{\rm gas}(r)$, determined from the Chandra data is shown in Fig. 9. Within a scale radius, $r_s \sim 0.7$ Mpc, the $f_{\rm gas}$ value rises with a slope $f_{\rm gas} \propto r^{0.3}$, although there is some evidence for a flattening of the curve towards larger radii. The measured $f_{\rm gas}$ value at $r = 0.9$ Mpc of $f_{\rm gas} = 15.7^{+5.6}_{-4.1}$ per cent (90 per cent confidence limits) is consistent with the previous measurement of 17.5 ± 2.4 per cent (1σ limits) at $r = 1$Mpc by Ettori & Fabian (1999), using ROSAT PSPC and ASCA data and assuming isothermality in the X-ray gas.

Following the usual arguments, which assume that the properties of clusters provide a fair sample of those of the Universe as a whole (*e.g.* White *et al.* 1993; White & Fabian 1995; Evrard 1997; Ettori & Fabian 1999; Bahcall *et al.* 1999), we may use our result on the X-ray gas mass fraction in Abell 2390 to estimate the total matter density in the Universe, $\Omega_{\rm m}$. Assuming that the luminous baryonic mass in galaxies in Abell 2390 is approximately one fifth of the X-ray gas mass (*e.g.* White *et al.* 1993; Fukugita, Hogan & Peebles 1998) and neglecting other possible sources of baryonic dark matter in the cluster, we obtain $\Omega_{\rm m} = (\Omega_{\rm b}/1.2 f_{\rm gas}) h_{50}^{-0.5}$, where $\Omega_{\rm b}$ is mean baryon density in the Universe and h_{50} is the Hubble constant in units of 50 km s^{-1} Mpc^{-1}. For $\Omega_{\rm b} h_{50}^2 = 0.05 \pm 0.03$ (*e.g.* see discussion in Ettori & Fabian 1999), $\Omega_{\rm m} = 0.27 \pm 0.18 h_{50}^{-0.5}$.‡

6 THE PROPERTIES OF THE COOLING FLOW

6.1 Radial properties of the cluster gas

The results on the electron density and cooling time as a function of radius, determined from the image deprojection analysis using the best-fit NFW mass model, are shown in Fig. 10. Within the central 500 kpc radius, the electron density profile can be well-modelled ($\chi^2 = 33.1$ for 51 degrees of freedom) by a β-profile with a core radius, $r_c = 21 \pm 4$ kpc, $\beta = 0.37 \pm 0.02$ and a central density, $n_{\rm e}(0) = 7.1 \pm 0.9 \times 10^{-2}$ cm^{-3} (1σ errors). We note, however, that this model slightly underestimates the electron density in the innermost bin (by ~ 20 per cent). The core radius for the electron density distribution is smaller than the value measured directly from the projected surface brightness profile under the assumption of strict isothermality in the X-ray gas (Section 3.2). Indeed, the evidence for any flat central core in the electron density distribution is marginal and a simple broken power-law model, with $r_{\rm break} = 56^{+11}_{-12}$ kpc and slopes interior and exterior to the break radius of -0.54 ± 0.05 and -1.13 ± 0.05, provides as good a fit to the electron density profile in the central 500 kpc region ($\chi^2 = 30.6$ for 50 degrees of freedom).

For an assumed Galactic column density of 6.8×10^{20}atom cm^{-2}, we measure a central cooling time (*i.e.* the mean cooling time within the central 1.97 arcsec or (~ 9 kpc) bin of $t_{\rm cool} = 3.7^{+1.6}_{-0.9} \times 10^8$ yr, and a cooling radius, at which the cooling time first exceeds a Hubble time, of $r_{\rm cool} = 173^{+60}_{-4}$ kpc. (Errors on the central cooling time are the 10 and 90 percentile values from 100 Monte Carlo simulations. The upper and lower confidence limits on the cooling radii are the points where the 10 and 90 percentile values exceed and become less than the Hubble time, respectively.)

‡ Accounting for any additional, dark baryonic matter in the cluster would lower the measured value of $\Omega_{\rm m}$. Likewise, if the value of $f_{\rm gas}$ increases towards larger radii in Abell 2390, the true value for $\Omega_{\rm m}$ will be lower than our quoted result.

6.2 X-ray colour profile analysis

We have constructed an X-ray 'colour' profile for the cluster in order to determine the size of the central region in which significant cooling occurs. Two separate images were created in the energy bands $0.5 - 1.3$ and $1.3 - 7.0$ keV ($0.62 - 1.60$ and $1.6 - 8.6$ keV in the rest frame of the source) with a 1.97 arcsec (4 raw detector pixels) pixel scale. These soft and hard X-ray images were background subtracted and flat fielded (taking full account of the spectral energy distributions of the detected photons). All significant point sources were masked out and excluded from the analysis. Azimuthally-averaged surface-brightness profiles for the cluster were then constructed in each energy band, centered on the overall peak of the X-ray emission (Section 3). The X-ray 'colour' profile formed from the ratio of the surface brightness profiles in the soft and hard bands is shown in Fig. 11.

From examination of Fig. 11 we see that at large radii the observed X-ray colour ratio is approximately constant, with a mean value of 1.01 ± 0.03 (1σ error determined from a fit to the data between radii of $150 - 300$ kpc). By comparison with simulated spectra we find that this result is consistent with an isothermal plasma with a temperature $kT = 11.0 \pm 1.5$ keV. (We assume a metallicity $Z \sim 0.4Z$ and Galactic absorption.) Within a 'break' radius of 70^{+20}_{-12} kpc (1σ errors determined from a χ^2 fit with a broken power-law model), however, the colour ratio rises sharply, indicating the presence of significantly cooler gas. This break radius may be plausibly associated with the outer edge of the cooling flow.

6.3 Analysis of the mass deposition profile

The outermost radius at which cooling occurs may also be expected to be associated with a 'break' in the X-ray surface brightness profile and, more evidently, the mass deposition profile determined from the deprojection code. The mass deposition profile from the cooling flow, which is a parameterization of the X-ray luminosity distribution in the cluster core (see *e.g.* White *et al.* 1997), is shown in Fig. 12. Fitting this profile with simple a broken power-law model, we determine a break radius of 58^{+24}_{-19} kpc (1σ errors), in good agreement with the break radius determined from the fit to the X-ray colour profile (Section 6.2) and the electron density distribution (Section 6.1) . The best-fit broken power-law model is shown overlaid on the mass deposition profile in Fig. 12.

The slopes of the mass deposition profile, internal and external to the break radius are $1.60^{+0.19}_{-0.15}$ and $0.82^{+0.17}_{-0.18}$, respectively. Accounting only for absorption due to cold gas with the nominal Galactic column density, we determine an integrated mass deposition rate within the break radius in the mass deposition profile of $176^{+59}_{-82}\,\mathrm{M_\odot\,yr^{-1}}$. Similarly, the mass deposition rate within the break radius identified from the X-ray colour profile is $206^{+48}_{-29}\,\mathrm{M_\odot\,yr^{-1}}$. If we also account for the presence of intrinsic absorption on these results, with the properties determined using spectral model C2(iii), the mass deposition rates within the respective break radii rise to 191^{+64}_{-89} and $224^{+52}_{-32}\,\mathrm{M_\odot\,yr^{-1}}$, respectively. These results are in good agreement with the independent value determined from the spectral analysis of $242^{+61}_{-56}\,\mathrm{M_\odot\,yr^{-1}}$ (using our preferred spectral model c2(iii)).

6.4 The age of the cooling flow

Allen *et al.* (2000a) discuss a number of methods which may be used to estimate the ages of cooling flows from the X-ray data. (Such ages are likely to relate to the time intervals since the central regions of clusters were last disrupted by major subcluster merger events.) Essentially, these methods identify the age of a cooling flow with the cooling time of the X-ray gas at the break radius in either the X-ray colour or deprojected mass deposition profile.

Using Fig. 10(b), we see that cooling time of the X-ray gas at the break radius in the X-ray colour profile (70^{+20}_{-12} kpc) lies in the range $3.15^{+0.80}_{-0.48}$ Gyr. (The cooling time at the break radius is measured from a least-squares fit to the data in Fig. 10(b) using a power-law model.) If we instead identify the age of the cooling flow with the cooling time at the break radius in the mass deposition profile in Fig. 12 (58^{+24}_{-19} kpc), we infer an age for the cooling flow of $2.65^{+0.96}_{-0.77}$ Gyr. (In both cases we assume that no intrinsic absorption acts beyond the outer edge of the cooling flow, which is reasonable if the absorbing matter is accumulated by the flow.)

In summary, we see the X-ray colour profile, image deprojection analysis and spectral data provide consistent results on the properties of the cooling flow in Abell 2390, indicating a mass deposition rate in the range $200 - 250$ $\mathrm{M_\odot\,yr^{-1}}$ and an age of ~ 3.0 Gyr.

6.5 On the rising ambient temperature profile within the cluster core

In principle, the results on the X-ray gas temperature and surface brightness within the cluster core may be used to distinguish between an NFW model for the dark matter distribution and alternative models with a steeper central cusp (*e.g.* Moore *et al.* 1999). The results for Abell 2390 presented here are certainly consistent with an NFW profile (see Fig. 7). However, given the complexity of the gas within the central 100 kpc and the relatively short exposure time of the present observation (which limits the number of independent spectra which can be extracted from the region of the cluster core), we do not attempt to explore these other models here. This issue will be better addressed with Chandra data for nearer, brighter systems.

The fact that the ambient temperature profile, corrected for the effects of the cooling flow, rises with increasing radius throughout the central ~ 200 kpc, is interesting. In detail, the density and temperature structure in the cluster core will depend on the thermal history of the gas, as well as the underlying dark matter distribution and, subject to pressure equilibrium and convective stability, may be flat, increase or decrease with radius. As discussed in Section 4.6, the presence of relatively cool, ambient gas in the central regions of Abell 2390 may have lead to overestimates of the mass deposition rate in previous studies with ASCA and Beppo-SAX in which this region was not spatially resolved.

There are several reasons why relatively cool, dense gas

might exist beyond the outer edge of the present-day cooling flow in Abell 2390. The first is that a pre-existing cooling flow may have been disturbed several Gyr ago. Cooler, denser gas could then have been spread out over several 100 kpc, with the cooling flow having so far only re-established itself within the inner ~ 70 kpc. A second possibility is that the densest gas from the cores of infalling subclusters may have been stripped and deposited over time in the core of the main cluster without strong shocking (Fabian & Daines 1991). The situation seen in the Chandra data for Abell 2142 (Markevitch *et al.* 2000) is reminiscent of this, with a sharp drop in temperature from $kT \sim 14$ keV to $kT \sim 7$ keV (and a corresponding rise in density) observed at $r \sim 370$ kpc, moving inwards from northwest of the cluster centre. Such a sharp drop in temperature at these radii cannot be due to any current cooling flow in the cluster.

7 CONCLUSIONS

The main conclusions from this work may be summarized as follows:

(i) We have measured the distribution of mass in Abell 2390 using Chandra X-ray observations. The mass profile can be well-modelled by an NFW profile with a scale radius $r_{\rm s} \sim 0.7$ Mpc and a concentration parameter, $c \sim 5$. The normalization of the mass profile may also be expressed in terms of an equivalent velocity dispersion, $\sigma = \sqrt{50} H_0 r_{\rm s} c = 1260^{+130}_{-110}\,{\rm km\,s^{-1}}$ (assuming a fixed value for $r_{\rm s} = 0.7$ Mpc), in excellent agreement with the optically-determined value of $1262^{+89}_{-68}\,{\rm km\,s^{-1}}$ (Borgani *et al.* 1999).

(ii) The best-fit Chandra mass model is in excellent agreement with independent measurements from strong and weak lensing studies. The mean scatter between the X-ray and lensing values is < 20 per cent.

(iii) The X-ray gas to total mass ratio rises with increasing radius within the central 0.7 Mpc radius with $f_{\rm gas} \propto r^{0.3}$. At $r = 0.9$ Mpc we measure $f_{\rm gas} = 15.7^{+5.6}_{-4.1}$ per cent (90 per cent confidence limits). Following the usual arguments, this result on the X-ray gas mass fraction may be converted into a constraint on the mean mass density in the Universe, $\Omega_{\rm m} = 0.27 \pm 0.18 h_{50}^{-0.5}$.

(iv) The X-ray gas temperature rises with increasing radius within the central ~ 200 kpc, and then remains approximately isothermal with $kT = 11.5^{+1.6}_{-1.3}$ keV out to $r \sim 1.0$ Mpc. The drop in the emission weighted temperature in the central 100 kpc region is in part, but not entirely, due to the presence of the central cooling flow.

(v) The best-fit mass deposition rate from the cooling flow, determined in a consistent manner from the spectral and imaging Chandra data, lies in the range $200 - 250$ ${\rm M_\odot\,yr^{-1}}$. This value is lower than previous estimates based on integrated ASCA and Beppo-SAX spectra for the entire cluster, which could not resolve the drop in the central, ambient gas temperature. We estimate an age for the cooling flow in Abell 2390 of ~ 3 Gyr.

(vi) The azimuthally-averaged $0.3 - 7.0$ keV surface brightness profile exhibits a small core radius and a clear break at $r \sim 0.5$ Mpc, where the slope changes abruptly from $S_{\rm X} \propto r^{-1.4}$ to $S_{\rm X} \propto r^{-3.7}$.

Acknowledgements

We thank G. Squires for communicating his weak lensing results and P. Thomas for discussions. We thank R. Johnstone and R. Schmidt for coding and discussions regarding the analysis of Chandra data. We acknowledge the support of the Royal Society.

REFERENCES

Akritas M.G., Bershady M.A., 1996, ApJ, 470, 706
Allen S.W., 1998, MNRAS, 296, 392
Allen S.W., 2000, MNRAS, 315, 269
Allen S.W., Fabian A.C., 1997, MNRAS, 286, 583
Allen S.W., Fabian A.C., 1998, MNRAS, 297, L57
Allen S.W., Fabian A.C., Kneib J.-P., 1996, MNRAS, 279, 615
Allen S.W., Fabian A.C., Johnstone R.M., Nulsen P.E.J., Arnaud K.A., 2000a, MNRAS, submitted
Allen S.W. *et al.* 2000b, MNRAS, submitted
Anders E., Grevesse N., 1989, Geochemica et Cosmochimica Acta 53, 197
Arnaud, K.A., 1996, in Astronomical Data Analysis Software and Systems V, eds. Jacoby G. and Barnes J., ASP Conf. Series volume 101, p17
Arnaud K.A., Mushotzky R.F., 1998, ApJ, 501, 119
Bacon D.J., Refregier A., Clowe D., Ellis R., 2000, MNRAS, in press (astro-ph/0007023)
Bahcall N.A., Ostriker J.P., Perlmutter S., Steinhardt P.J., 1999, Science, 284, 1481
Balucinska-Church M., McCammon D., 1992, ApJ, 400, 699
Bartelmann M., Steinmetz M., 1996, MNRAS, 283, 431
Bartelmann M., Schneider P., preprint (astro-ph/9912508)
Bezecourt J., Soucail G., 1997, A&A, 317, 661
Böhringer H., Tanaka Y., Mushotzky R.F., Ikebe Y., Hattori M., 1998, A&A, 334, 789
Borgani S., Girardi M., Carlberg R.G., Yee H.K.C., Ellingson E., 1999, ApJ, 527, 561
Buote D.A., 2000, ApJ, 532, L113
Buote D.A., Tsai J.C., 1996, ApJ, 458, 27
Carlberg R.G., Yee H.K.C., Ellingson E., Abraham R., Gravel P., Morris S., Pritchet C.J., 1996, ApJ, 462, 32
de Grandi S., Molendi S., 1999, ApJ, 527, L25
den Hartog R., Katgert P., 1996, MNRAS, 279, 349
Dickey J.M., Lockman F.J., 1990, ARA&A, 28, 215
Ebeling H., Rangarajan F.V.N., White D.A., 2000, MNRAS, in press
Edge A.C., Stewart G.C., Fabian A.C., 1992, MNRAS, 255, 431
Edge A.C., Ivison R.J., Smail I., Blain A.W., Kneib J.-P., 1999, MNRAS, 306, 599
Ettori S., Fabian A.C., 1999, MNRAS, 305, 834
Ettori S., Allen S.W., Fabian A.C., 2000, MNRAS, submitted
Evrard A.E., 1997, MNRAS, 292, 289
Fabian A.C., Daines S.J., 1991, MNRAS, 252, L17
Fabian A.C., Hu E.M., Cowie L.L., Grindlay J., 1981, ApJ, 248, 47
Fabian A.C. *et al.* 2000a, MNRAS, 315, L8
Fabian A.C. *et al.* 2000b, MNRAS, submitted
Fadda D., Girardi M., Giuricin G., Mardirossian F., Mezzetti M., 1996, ApJ, 473, 670
Fort B., Mellier Y., 1994, A&AR, 5, 239
Frenk C.S., White S.D.M., Efstathiou G., Davis M., 1990, ApJ, 351, 10
Frye B., Broadhurst T., 1998, ApJL, 499, 115
Fukugita M., Hogan C.J., Peebles P.J.E., 1998, ApJ, 503, 518
Geller M.J., Diaferio A., Kurtz M.J., 1999, ApJ, 517, 23
Hutchings J.B., Balogg M.L., 2000, AJ, 119, 1123

Irwin J.A., Bregman J.N., 2000, ApJ, 538, 543
Johnstone R.M., Fabian A.C., Edge A.C., Thomas P.A., 1992, MNRAS, 255, 431
Jones C., Forman W., 1984, ApJ, 276, 38
Kaastra J.S., Mewe R., 1993, Legacy, 3, HEASARC, NASA
Kassiola A., Kovner I., Blandford R.D., 1992, ApJ, 396, 10
Kikuchi K., Tae F., Ezawa H., Yamasaki N.Y., Ohashi T., Fukazawa Y., Ikebe Y., 1999, PASJ, 51, 301
Kneib J.-P., Mellier Y., Pelló R., Miralda-Escudé J., Le Borgne J.-F., Böhringer H., Picat J.-P., 1995, A&A, 303,27
Koranyi D.M., Geller M.J., 2000, AJ, 119, 44
Lemonon L., Pierre M., Cesarsky C.J., Elbaz D., Pelló R., Soucail G., Vigroux L., 1998, A&A, 334, L21
Lewis A.D., Ellingson E., Morris S.L., Carlberg R.G., 1999, 517, 587
Liedhal D.A., Osterheld A.L., Goldstein W.H., 1995, ApJ, 438, L115
Loeb A., Mao, S., 1994, ApJ, 435, 109L
Lucey J.R., 1983, MNRAS, 204, 33
Markevitch M., Forman W.R., Sarazin C.L., Vikhlinin A., 1998, ApJ, 503, 77
Markevitch M. *et al.* , 2000, ApJ, in press (astro-ph/0001269)
Mazure A., *et al.* , 1996, A&A, 310, 31
McNamara B.R. *et al.* , 2000, ApJL, 534, 135
Mellier Y., 1999, ARA&A, 37, 127
Miralda-Escudé J., Babul A., 1995, ApJ, 449, 18
Moore B., Quinn T., Governato F., Stadel J., Lake G., 1999, MNRAS, 310, 1147
Narasimha D., Chitre S.M., 1993, A&A, 280, 57
Navarro J.F., Frenk C.S., White S.D.M., 1997,ApJ, 490, 493
Nulsen P.E.J., 1998, MNRAS, 297, 1109
Pelló R., Sanahuja B., Le Borgne J.F., Soucail G., Mellier Y., 1991, ApJ, 366, 405
Pelló R. *et al.* , 1999, A&A, 346, 359
Pierre M., Le Borgne J.F., Soucail G., Kneib J.-P., 1996, A&A, 311, 413
Roettiger K., Burns J.O., Loken C., 1996, ApJ, 473, 651
Sarazin C.L., 1988, X-ray emission from clusters of galaxies. Cambridge Univ. Press, Cambridge
Smail I., Couch W.J., Ellis R.S., Sharples R.M., 1995, ApJ, 440, 501
Smail I., Ellis R.E., Dressler A., Couch W.J., Oemler A. Sharples R.M., Butcher H., 1997, ApJ, 479, 70
Squires G., Kaiser N., Babul A., Fahlman G., Woods D., Neumann D.M., Böhringer H., 1996, ApJ, 461, 572
Squires G., Neumann D.M., Kaiser N., Arnaud M., Babul A., Böhringer H., Fahlman G., Woods D., 1997, ApJ, 482, 648
Thomas P.A., Muanwong O., Pearce F.R., Couchman H.M.P., Edge A.C., Jenkins A., Onuora L., 2000, MNRAS, submitted (astro-ph/0007348)
van Haarlem M.P., Frenk C.S., White S.D.M., 1997, MNRAS, 287, 817
Waxman E., Miralda-Escudé J., 1995, ApJ, 451, 451
Weisskopf M.C., Tananbaum H.D., Van Speybroeck L.P., O'Dell S.L., 2000, SPIE 4012, 1 (astro-ph/0004127)
White D.A., 2000, MNRAS, 312, 663
White D.A., Fabian A.C., 1995, MNRAS, 273, 72
White D.A., Jones C., Forman W., 1997, MNRAS, 292, 419
White S.D.M., Efstathiou G., Frenk C.S., 1993, MNRAS, 262, 1023
Wise M.W., Sarazin C.L., 2000, ApJ, in press (astro-ph/9903119)
Wu X., Fang L., 1997, ApJ, 483, 62
Wu X., 2000, MNRAS, in press (astro-ph/0006124)

Table 1. The results from the analysis of the annular spectra using spectral model A in the $0.5-7.0$ keV band. Temperatures (kT) are in keV, metallicities (Z) in solar units and normalizations (K) in units of $(10^{-17}/(4\pi(D_{\rm A}(1+z))^2))\int n_{\rm e}n_{\rm H}dV$, where $D_{\rm A}$ is the angular size distance to the source in cm, $n_{\rm e}$ is the electron density (in cm^{-3}), and $n_{\rm H}$ is the hydrogen ion density (in cm^{-3}). The absorbing column density has been fixed at the nominal Galactic value of 6.8×10^{20}atom cm^{-2}. The total χ^2 values and number of degrees of freedom (DOF) in the fits are listed in column 5. Error bars at both the 1σ ($\Delta\chi^2=1.0$) and 90 per cent ($\Delta\chi^2=2.71$; in parentheses) confidence limits on a single interesting parameter are listed. For the outermost $0.7-1.0$ Mpc annulus, where the instrumental background is most significant, only data in the energy range $0.5-6.0$ keV range were used.

Model A	kT	Z	K	χ^2/DOF
$0-50$	$5.58^{+0.52(+0.93)}_{-0.42(-0.65)}$	$0.48^{+0.16(+0.29)}_{-0.18(-0.29)}$	$1.48^{+0.07(+0.11)}_{-0.06(-0.10)}$	98.2/79
$0-100$	$6.81^{+0.43(+0.74)}_{-0.39(-0.62)}$	$0.48^{+0.11(+0.18)}_{-0.10(-0.17)}$	$3.41^{+0.08(+0.14)}_{-0.09(-0.14)}$	132.5/123
$0-200$	$7.97^{+0.45(+0.77)}_{-0.42(-0.67)}$	$0.36^{+0.08(+0.13)}_{-0.08(-0.13)}$	$6.49^{+0.11(+0.19)}_{-0.12(-0.19)}$	159.7/163
$50-100$	$8.58^{+1.07(+1.86)}_{-0.85(-1.31)}$	$0.55^{+0.19(+0.33)}_{-0.19(-0.31)}$	$1.86^{+0.07(+0.11)}_{-0.07(-0.12)}$	96.9/98
$100-150$	$9.54^{+1.45(+2.60)}_{-1.10(-1.72)}$	$0.21^{+0.17(+0.29)}_{-0.17(-0.21)}$	$1.62^{+0.07(+0.10)}_{-0.06(-0.09)}$	78.9/82
$150-200$	$8.94^{+1.40(+2.64)}_{-1.06(-1.62)}$	$0.48^{+0.28(+0.47)}_{-0.27(-0.45)}$	$1.32^{+0.07(+0.12)}_{-0.11(-0.07)}$	69.0/74
$100-200$	$9.40^{+0.97(+1.75)}_{-0.82(-1.28)}$	$0.28^{+0.14(+0.24)}_{-0.14(-0.23)}$	$2.98^{+0.09(+0.15)}_{-0.09(-0.14)}$	128.9/121
$200-300$	$12.03^{+1.93(+3.45)}_{-1.60(-2.42)}$	$0.26^{+0.23(+0.38)}_{-0.24(-0.26)}$	$2.35^{+0.11(+0.16)}_{-0.09(-0.15)}$	106.7/108
$300-400$	$10.84^{+1.76(+3.40)}_{-1.39(-2.13)}$	$0.37^{+0.25(+0.40)}_{-0.25(-0.37)}$	$2.07^{+0.11(+0.17)}_{-0.09(-0.14)}$	100.6/105
$400-500$	$12.46^{+2.33(+4.30)}_{-1.77(-2.70)}$	$0.00^{+0.10(+0.23)}_{-0.00(-0.00)}$	$1.73^{+0.04(+0.07)}_{-0.04(-0.07)}$	89.1/88
$500-700$	$9.73^{+1.56(+2.80)}_{-1.19(-1.81)}$	$0.49^{+0.27(+0.46)}_{-0.26(-0.44)}$	$2.14^{+0.11(+0.19)}_{-0.10(-0.16)}$	62.5/67
$700-1000$	$13.08^{+4.51(+8.49)}_{-2.81(-3.99)}$	$0.55^{+0.61(+1.06)}_{-0.55(-0.55)}$	$1.37^{+0.14(+0.21)}_{-0.11(-0.18)}$	46.1/52
$200-1000$	$11.46^{+0.95(+1.62)}_{-0.79(-1.26)}$	$0.23^{+0.12(+0.20)}_{-0.13(-0.21)}$	—	410.4/428

Table 2. The results from the analysis of the annular spectra in the $0.5-7.0$ keV band using spectral model B. The absorbing column density ($N_{\rm H}$) is in units of 10^{20} atom cm^{-2}. Other details as in Table 1.

Model B	kT	Z	$N_{\rm H}$	χ^2/DOF
$0-50$	$4.77^{+0.47(+0.82)}_{-0.40(-0.63)}$	$0.48^{+0.16(+0.26)}_{-0.14(-0.23)}$	$9.86^{+1.25(+2.08)}_{-1.24(-2.00)}$	91.8/78
$0-100$	$6.18^{+0.49(+0.83)}_{-0.41(-0.66)}$	$0.45^{+0.09(+0.16)}_{-0.10(-0.16)}$	$8.71^{+0.95(+1.58)}_{-0.94(-1.53)}$	128.3/122
$0-200$	$7.19^{+0.50(+0.87)}_{-0.44(-0.70)}$	$0.33^{+0.07(+0.12)}_{-0.07(-0.11)}$	$8.35^{+0.71(+1.17)}_{-0.70(-1.14)}$	154.7/162
$50-100$	$7.46^{+1.06(+1.97)}_{-0.77(-1.21)}$	$0.49^{+0.18(+0.30)}_{-0.16(-0.26)}$	$8.83^{+1.31(+2.18)}_{-1.32(-2.16)}$	94.5/97
$100-150$	$8.31^{+1.52(+2.83)}_{-1.19(-1.84)}$	$0.22^{+0.15(+0.25)}_{-0.16(-0.22)}$	$8.48^{+1.42(+2.37)}_{-1.37(-2.22)}$	77.3/81
$150-200$	$8.32^{+1.68(+3.30)}_{-1.15(-1.74)}$	$0.47^{+0.26(+0.45)}_{-0.25(-0.41)}$	$7.78^{+1.58(+2.63)}_{-1.56(-2.53)}$	68.6/73
$100-200$	$8.62^{+1.14(+2.06)}_{-0.91(-1.40)}$	$0.28^{+0.13(+0.21)}_{-0.13(-0.21)}$	$7.90^{+1.06(+1.75)}_{-1.04(-1.69)}$	127.8/120
$200-300$	$12.03^{+2.79(+5.16)}_{-2.20(-3.17)}$	$0.26^{+0.22(+0.38)}_{-0.24(-0.26)}$	$6.80^{+1.30(+2.15)}_{-1.18(-1.95)}$	106.7/107
$300-400$	$8.79^{+1.74(+3.26)}_{-1.20(-1.85)}$	$0.41^{+0.20(+0.33)}_{-0.20(-0.34)}$	$8.97^{+1.35(+2.26)}_{-1.35(-2.22)}$	98.0/104
$400-500$	$12.52^{+3.52(+7.23)}_{-2.32(-3.49)}$	$0.00^{+0.10(+0.23)}_{-0.00(-0.00)}$	$6.76^{+1.51(+2.50)}_{-1.49(-2.47)}$	89.1/87
$500-700$	$10.23^{+2.49(+4.97)}_{-1.75(-2.55)}$	$0.48^{+0.29(+0.48)}_{-0.28(-0.43)}$	$6.34^{+1.34(+2.21)}_{-1.29(-2.11)}$	62.3/66
$700-1000$	$10.92^{+5.05(+11.0)}_{-2.42(-3.54)}$	$0.52^{+0.52(+0.99)}_{-0.46(-0.52)}$	$8.23^{+1.99(+3.34)}_{-2.04(-3.37)}$	45.5/51
$200-1000$	$10.87^{+1.19(+2.16)}_{-1.02(-1.59)}$	$0.25^{+0.11(+0.19)}_{-0.13(-0.21)}$	$7.28^{+0.66(+1.09)}_{-0.64(-1.06)}$	409.9/427

Table 3. The best-fit parameter values and 1σ (and 90 per cent; in parentheses) confidence limits determined from the multiphase analysis of the central 100 kpc region in the extended $0.3-7.0$ keV band. The mass deposition rates from the cooling flow ($\dot{M}$) are in units of $\mathrm{M}_{\odot}\,\mathrm{yr}^{-1}$. Column densities ($N_{\rm H}$) and intrinsic column densities ($\Delta N_{\rm H}$) are in units of 10^{20} atom cm^{-2}. The limits on the edge energy ($E_{\rm edge}$) determined with absorption model (v) are in keV. Other details as in Table 1.

		EMISSION MODEL		
		SINGLE-PHASE	MULTIPHASE	
ABSORPTION MODEL		A	C1	C2
	kT_1	$8.14^{+0.64(+1.14)}_{-0.56(-0.88)}$	$8.14^{+0.67(+1.36)}_{-0.56(-0.88)}$	$8.14^{+0.66(+1.43)}_{-0.56(-0.88)}$
CASE (i)	Z	$0.50^{+0.13(+0.21)}_{-0.13(-0.21)}$	$0.50^{+0.13(+0.21)}_{-0.12(-0.21)}$	$0.50^{+0.13(+0.21)}_{-0.12(-0.21)}$
GALACTIC ABSORPTION	$\dot{M}$	—	$0^{+17(+38)}_{-0(-0)}$	$0^{+17(+38)}_{-0(-0)}$
	χ^2/DOF	203.1/133	203.1/132	203.1/132
	kT_1	$5.78^{+0.39(+0.67)}_{-0.35(-0.57)}$	$6.59^{+0.78(+1.47)}_{-0.66(-1.00)}$	$6.45^{+0.73(+1.33)}_{-0.59(-0.90)}$
CASE (ii)	Z	$0.40^{+0.10(+0.16)}_{-0.07(-0.14)}$	$0.41^{+0.10(+0.17)}_{-0.15(-0.09)}$	$0.42^{+0.09(+0.16)}_{-0.10(-0.16)}$
VARIABLE ABSORPTION	$\dot{M}$	—	$109^{+58(+98)}_{-58(-94)}$	$109^{+60(+100)}_{-57(-93)}$
BY COLD GAS (z=0)	$N_{\rm H}$	$10.80^{+0.58(+0.96)}_{-0.56(-0.91)}$	$11.40^{+0.71(+1.19)}_{-0.68(-1.09)}$	$11.40^{+0.70(+1.19)}_{-0.68(-1.09)}$
	χ^2/DOF	141.6/132	137.9/131	137.9/131
	kT_1	$5.90^{+0.39(+0.67)}_{-0.35(-0.57)}$	$8.39^{+1.29(+2.47)}_{-0.88(-1.33)}$	$7.39^{+0.93(+1.75)}_{-0.58(-1.04)}$
CASE (iii)	Z	$0.41^{+0.10(+0.16)}_{-0.09(-0.14)}$	$0.44^{+0.11(+0.19)}_{-0.11(-0.18)}$	$0.43^{+0.11(+0.19)}_{-0.10(-0.17)}$
INTRINSIC ABSORPTION	$\dot{M}$	—	$270^{+40(+68)}_{-37(-61)}$	$242^{+37(+61)}_{-35(-56)}$
BY COLD GAS ($z=z_{\rm clus}$)	$\Delta N_{\rm H}$	$5.37^{+0.77(+1.27)}_{-0.75(-1.22)}$	$24.02^{+6.91(+12.14)}_{-5.96(-9.26)}$	$21.96^{+6.06(+10.75}_{-5.08(-7.92)}$
	χ^2/DOF	143.5/132	143.7/131	142.9/131
	kT_1	$5.90^{+0.39(+0.67)}_{-0.35(-0.57)}$	$8.38^{+1.30(+2.49)}_{-0.87(-1.32)}$	$7.45^{+0.88(+1.69)}_{-0.73(-1.10)}$
CASE (iv)	Z	$0.41^{+0.10(+0.16)}_{-0.09(-0.14)}$	$0.44^{+0.11(+0.19)}_{-0.11(-0.17)}$	$0.43^{+0.11(+0.19)}_{-0.10(-0.17)}$
PARTIAL COVERING	$\dot{M}$	—	$270^{+40(+65)}_{-37(-61)}$	$246^{+46(+112)}_{-38(-60)}$
BY COLD GAS ($z=z_{\rm clus}$)	$\Delta N_{\rm H}$	$5.37^{+0.77(+1.27)}_{-0.75(-1.22)}$	$24.07^{+6.86(+12.08)}_{-6.01(-9.31)}$	$21.35^{+8.38(+17.93)}_{-4.52(-7.37)}$
	f	$1.00^{+0.00(+0.00)}_{-0.29(-0.47)}$	$1.00^{+0.00(+0.00)}_{-0.16(-0.33)}$	$1.00^{+0.00(+0.00)}_{-0.17(-0.32)}$
	χ^2/DOF	143.5/131	143.7/130	142.9/130
	kT_1	$6.25^{+0.35(+0.71)}_{-0.36(-0.58)}$	$8.54^{+1.06(+1.93)}_{-0.81(-1.25)}$	$7.67^{+0.81(+1.50)}_{-0.67(-1.04)}$
CASE (v)	Z	$0.41^{+0.10(+0.16)}_{-0.09(-0.15)}$	$0.43^{+0.11(+0.19)}_{-0.12(-0.20)}$	$0.42^{+0.12(+0.20)}_{-0.11(-0.18)}$
SIMPLE EDGE	$\dot{M}$	—	$214^{+32(+55)}_{-29(-47)}$	$189^{+28(+46)}_{-27(-43)}$
($z=z_{\rm clus}$)	$E_{\rm edge}$	$0.43(<0.54)$	$<0.41(<0.43)$	$<0.41(<0.43)$
	τ	$1.02^{+0.21(+1.85)}_{-0.16(-0.26)}$	$17.7^{+6.89(+10.5)}_{-11.9(-13.4)}$	$15.5^{+5.9(+9.9)}_{-10.2(-11.5)}$
	χ^2/DOF	135.8/131	141.9/130	140.6/130

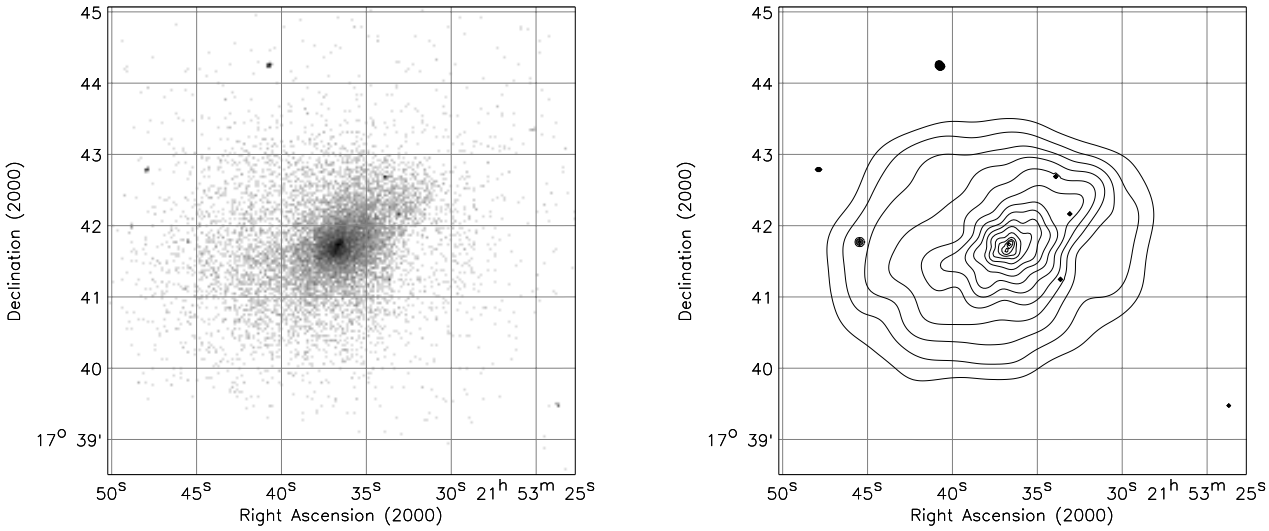

Figure 1. (Left panel) The raw $0.3 - 7.0$ keV Chandra image of Abell 2390. The pixel size is 2 detector pixels (0.9838 arcsec). (Right panel) Contour plot of the same region, adaptively smoothed using the code of Ebeling, White & Rangarajan (2000), with a threshold value of 3.5σ. The contours have equal logarithmic spacing.

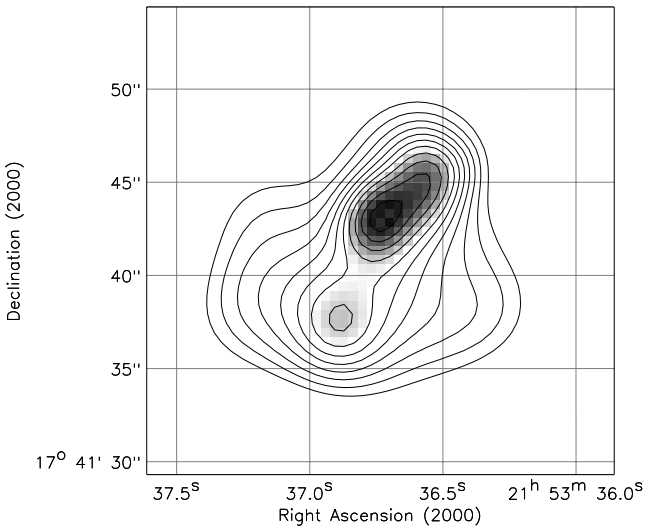

Figure 2. An adaptively smoothed $0.3 - 7.0$ keV image of the central regions of Abell 2390 on a finer spatial scale (pixel size 0.492×0.492 arcsec^2, which is equivalent to 1×1 raw detector pixels). Note the ridge of enhanced emission extending $\sim 3 - 4$ arcsec to the northwest of the X-ray peak which is coincident with the excess blue continuum and optical/UV line emission reported by Lémonon *et al.* (1998) and Hutchings & Balogh (2000).

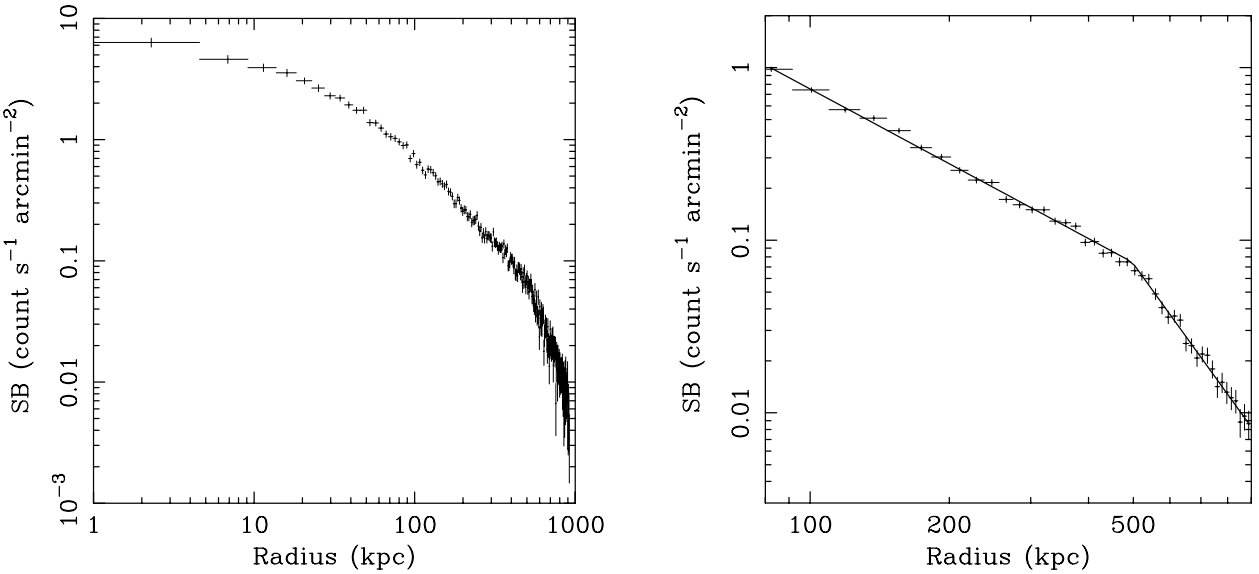

Figure 3. (a) The background-subtracted, flat-fielded, azimuthally-averaged radial surface brightness profile for Abell 2390 in the 0.3−7.0 keV band. The binsize is 0.984 arcsec (4.65 kpc). (b) The same profile, rebinned by a factor of 4, in the range $80 - 900$ kpc, with the best-fitting broken power-law model overlaid. At the break radius of 496^{+8}_{-14} kpc, the slope of the surface brightness profile ($S_{\rm X} \propto r^{\alpha}$) changes from $\alpha = -1.44 \pm 0.02$ to $\alpha = -3.71 \pm 0.16$.

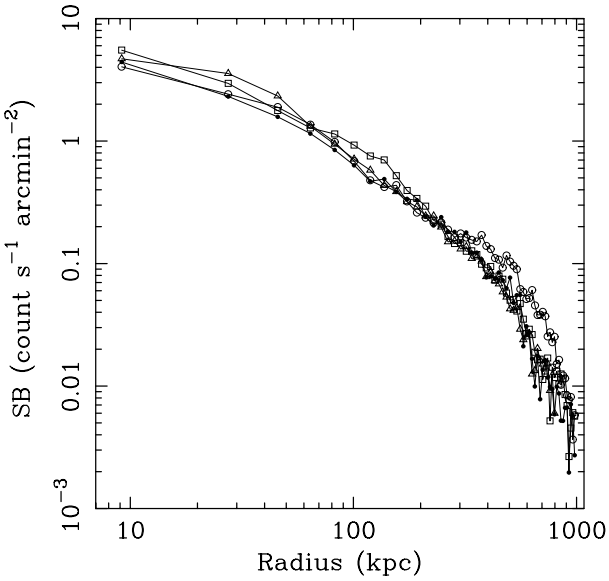

Figure 4. The $0.3 - 7.0$ keV surface brightness profile in quadrants covering position angles $315 - 45$ degrees (filled circles), $45 - 135$ degrees (open circles), $135 - 225$ degrees (triangles) and $225 - 315$ degrees (squares). The extension towards the East is also evident in Fig. 1. The results for the other quadrants are in good agreement with each other.

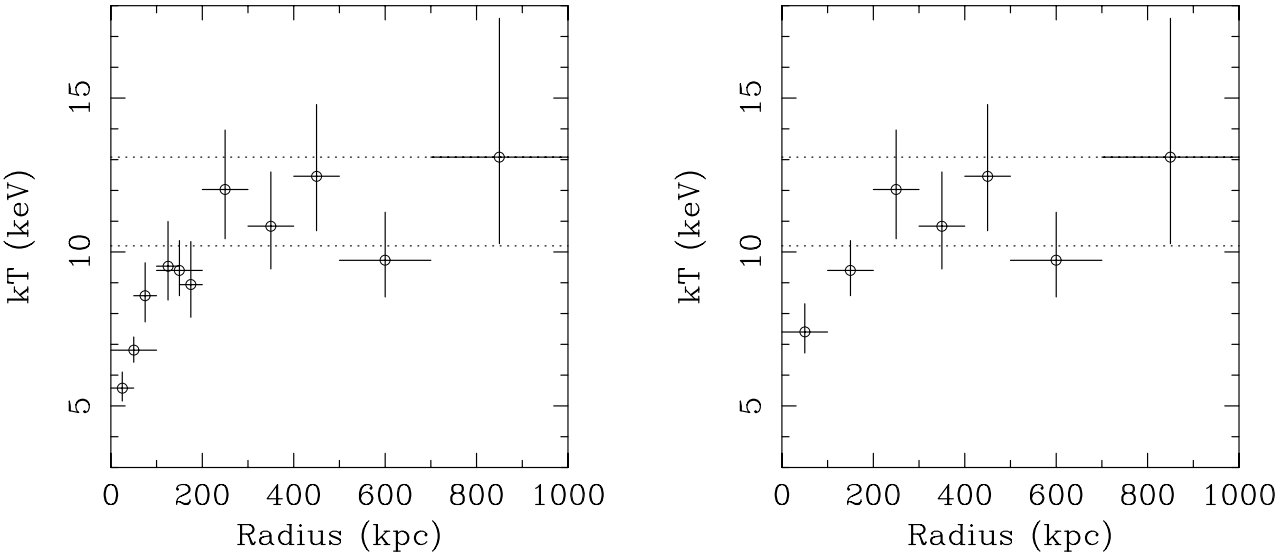

Figure 5. (a) The projected X-ray gas temperature profile (and 1σ errors) measured with spectral model A in the $0.5-7.0$ keV energy range. The dotted lines mark the 90 per cent confidence limits on the mean ambient cluster temperature determined from a joint analysis of the data in the $0.2-1.0$ Mpc region. (b) The ambient X-ray gas temperature as a function of radius, corrected for the effects of the cooling flow in the central 100kpc using spectral model C2(iii). For $r > 100$ kpc, the values are determined in an identical manner to those in (a).

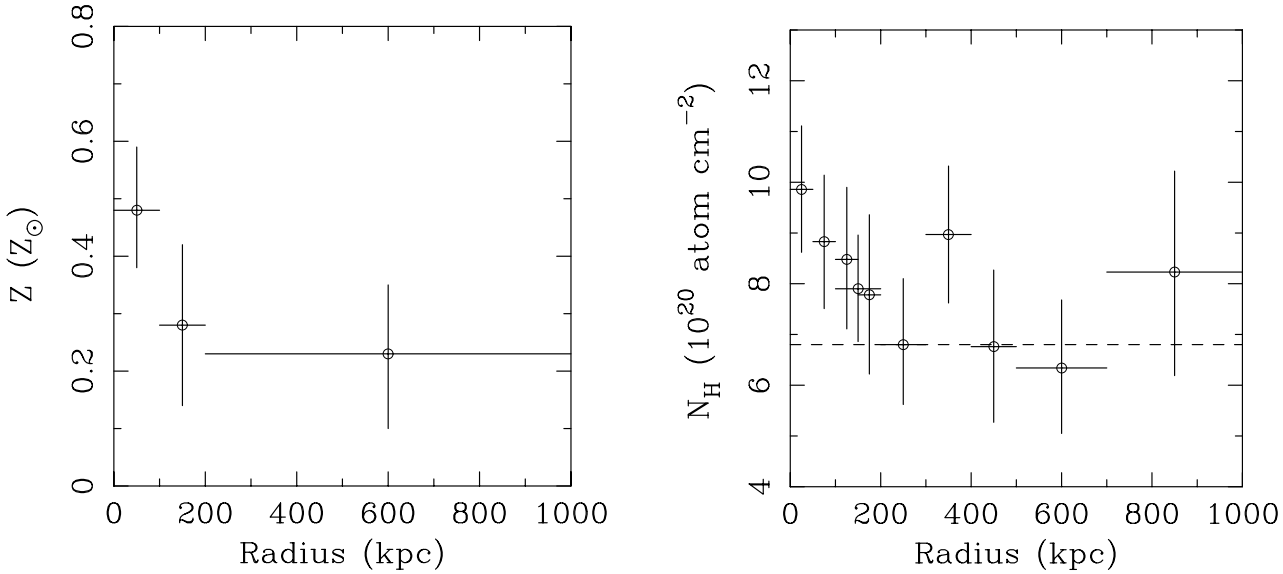

Figure 6. (a) The (projected) variation of metallicity in the cluster measured with spectral model A in the $0.5 - 7.0$ keV energy range. (b) The absorbing column density measured with spectral model B. The dashed line shows the Galactic column density determined from HI studies (Dickey & Lockman 1990).

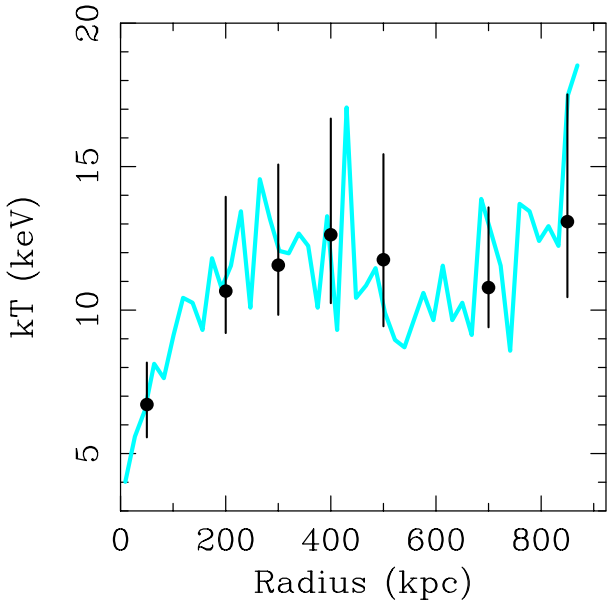

Figure 7. The deprojected X-ray gas temperature profile and 1σ errors (solid points) determined from the spectral deprojection analysis (Section 3.5) overlaid on the temperature profile determined from the image deprojection analysis using the best-fit NFW mass model (grey curve; Section 5. The median profile determined from 1000 monte-carlo simulations is shown). The agreement between the results demonstrates that the best-fit NFW mass model provides a reasonable description of the spatially-resolved Chandra spectra.

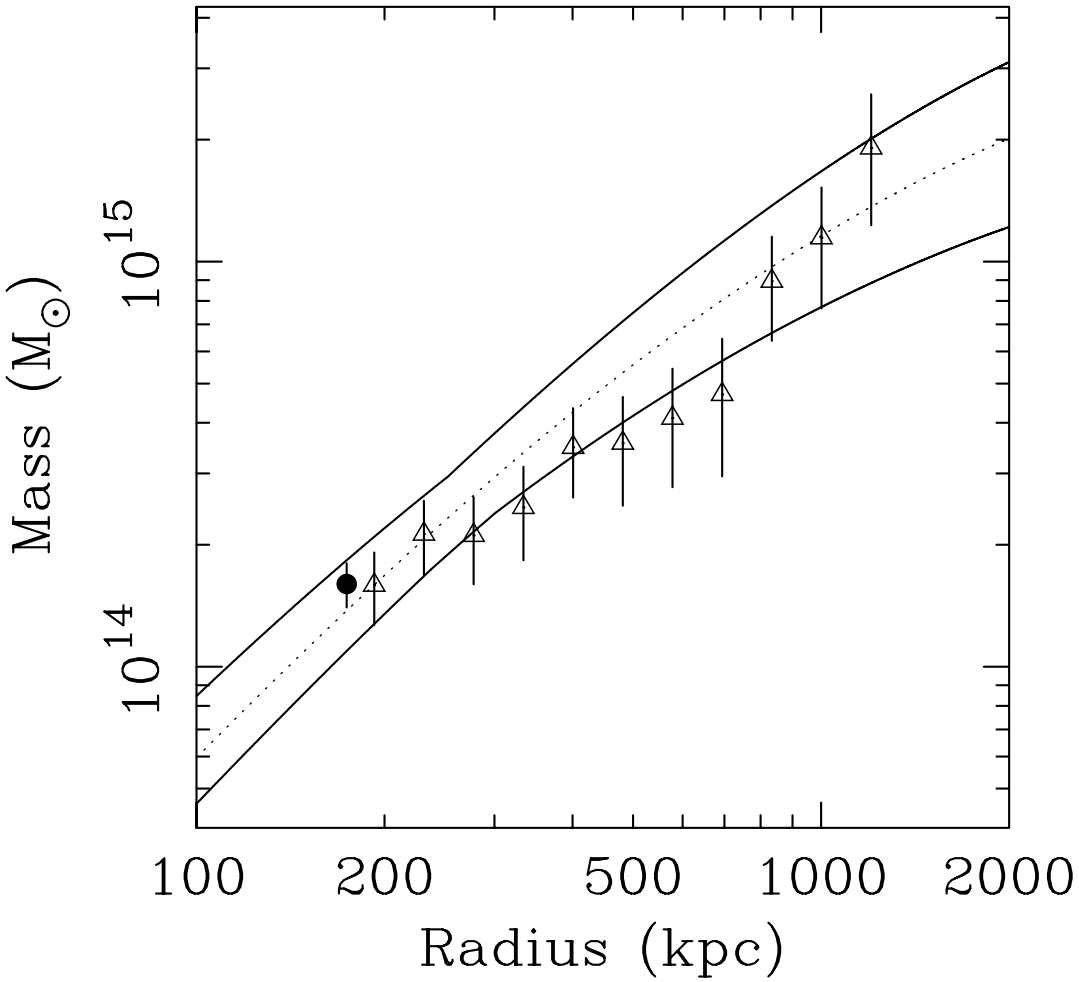

Figure 8. The comparison of the projected total mass determined from the Chandra X-ray data (Section 5) with the strong lensing result of Pierre *et al.* (1996; filled circle) and the weak lensing results of Squires *et al.* (1996; open triangles). The best-fit NFW X-ray mass model is shown as the dotted curve (parameters $r_{\rm s} = 700$ kpc, $\sigma = 1260\,{\rm km\,s^{-1}}$). The 90 percent confidence limits on the X-ray results, for $r_{\rm s}$ values in the range $0.4 - 1.0$ Mpc (see text), are shown as the solid curves.

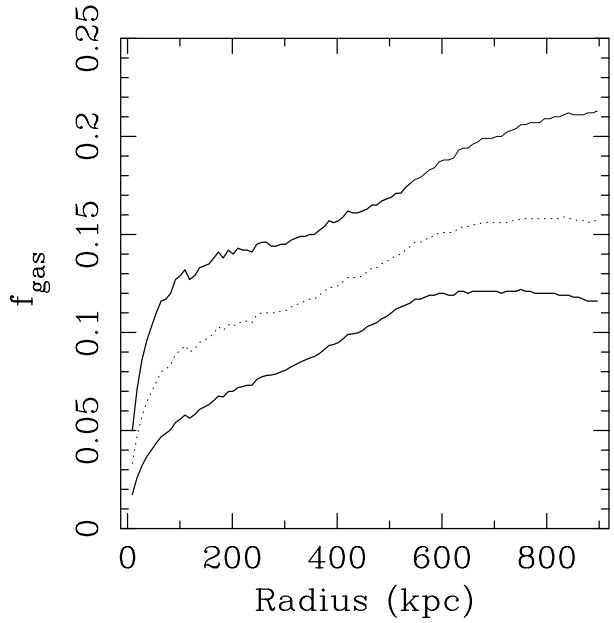

Figure 9. The ratio of the X-ray gas mass to total gravitating mass as a function of radius. The three curves, from top to bottom, show the 90 per cent confidence upper limit, best-fit value (dotted curve), and 90 per cent confidence lower limit. The data asymptote towards a best-fit value of $f_{\rm gas} = 0.157^{+0.056}_{-0.041}$ at $r \sim 0.9$ Mpc.

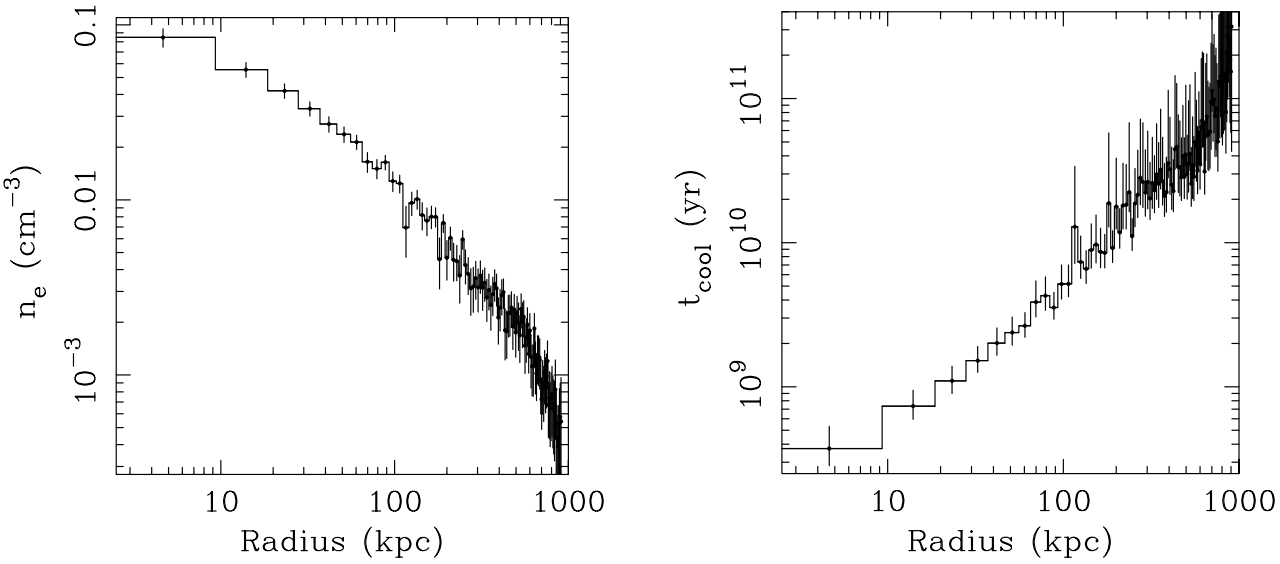

Figure 10. The results on (a) the electron density and (b) the cooling time, determined from the X-ray image deprojection analysis using the best-fit NFW mass model. Error bars are the 1σ errors determined from 1000 Monte Carlo simulations. A Galactic column density of 6.8×10^{20} atom cm^{-2} and a metallicity of 0.4 solar are assumed.

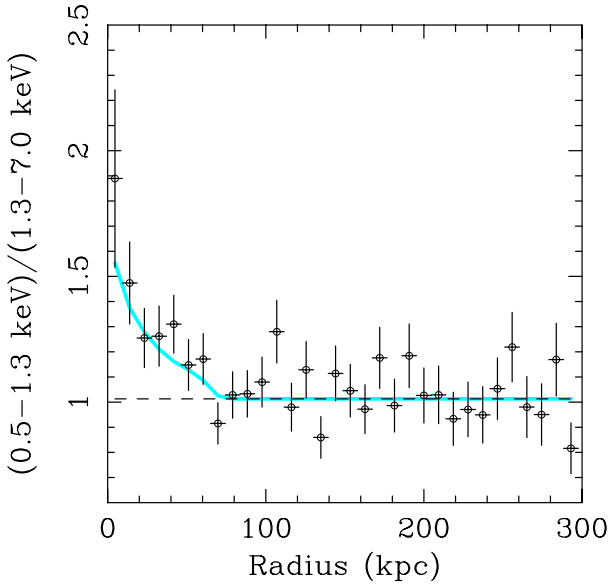

Figure 11. The X-ray colour profile, formed from the ratio of the counts in the $0.5-1.3$ and $1.3-7.0$ keV bands, as a function of radius. At large radii the ratio is approximately constant and consistent with a cluster temperature of 11.0 ± 1.5 keV. Within a 'break' radius of 70^{+20}_{-12} kpc, however, the colour ratio rises sharply. We associate the colour break radius with the outer edge of the cooling flow. Comparison with the cooling time curve shown in Fig. 10 suggests an age for the cooling flow of ~ 3.0 Gyr. The grey curve shows the predicted colour profile for a 3 Gyr old cooling flow from the image deprojection analysis (Sections 5,6) using the best-fit mass model and assuming that the cooling gas is intrinsically absorbed by a column density of 2.2×10^{21}atom cm^{-2}, as determined with spectral model C1(iii).

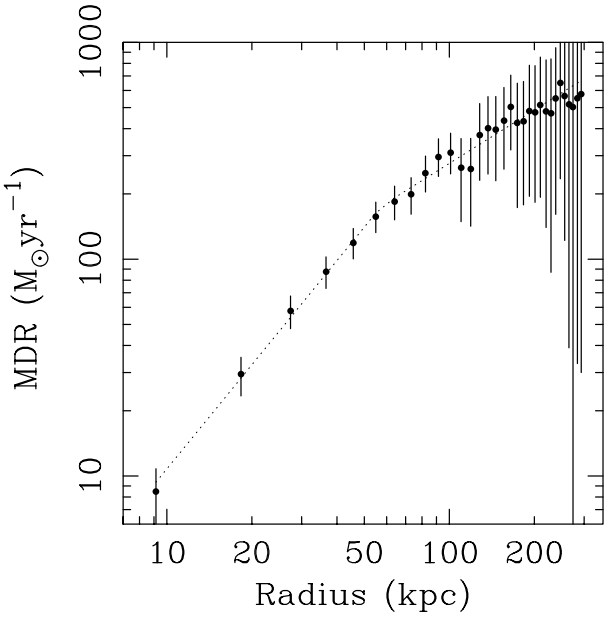

Figure 12. The mass deposition rate (MDR) in units of $M_\odot\,yr^{-1}$, determined from the image deprojection analysis using the best-fit NFW mass model. The dotted line is the best-fitting broken power-law model (Section 6.3). Error bars are the 10 and 90 percentile values from 1000 Monte Carlo simulations. A Galactic column density of 6.8×10^{20} atom cm^{-2}, a metallicity of 0.4 solar are assumed.